

A Family of Aperiodic Tilings with Tunable Quantum Geometric Tensor

Hector Roche Carrasco^{1,*}, Justin Schirrmann^{1,†}, Aurelien Mordret^{2,‡} and Adolfo G. Grushin^{1,§}

¹Univ. Grenoble Alpes, CNRS, Grenoble INP, Institut Néel, 38000 Grenoble, France

²Department of Geophysics and Sedimentary Basins,
Geological Survey of Denmark and Greenland (GEUS),
Øster Voldgade 10, 1350 Copenhagen K, Denmark

(Dated: June 12, 2025)

The strict geometric rules that define aperiodic tilings lead to the unique spectral and transport properties of quasicrystals, but also limit our ability to design them. In this work, we explore the first continuously tunable family of two-dimensional aperiodic tilings in which the underlying real-space geometry becomes a control knob of the wave-function's quantum geometric tensor. The real-space geometry can be used to tune into topological phases occupying an expanded phase space compared to crystals, or into a disorder-driven topological Anderson insulator. The quantum metric can also be tuned continuously, opening new routes towards tunable single- and many-body physics in aperiodic solid-state and synthetic systems.

Introduction—The electronic properties of quasicrystals can be strikingly different to those of crystals [1–3]. For example, quasicrystals exhibit rotational symmetries forbidden in crystals, and their wave-functions are neither localized nor extended [1–3]. However, the strict mathematical rules that determine the quasicrystalline atomic arrangements and the special wave-functions they host also restricts the possibility of tuning them. Different realizations of two-dimensional quasicrystals, such as the Penrose [4] or the Ammann-Beenker [5] tilings, cannot be smoothly deformed into one another. Hence, continuously tuning the electronic properties of quasicrystals is typically limited to changing model parameters, as in crystals [6–21].

A striking example of continuously tunable electronic properties are moiré heterostructures—stacks of two-dimensional materials rotated relative to each other by a twist angle [22–25]. Tuning this angle alters the real-space geometry, which in turn modifies the two components of the wavefunction's quantum geometric tensor, the quantum metric and Berry curvature [26–32]. The external control over this tensor has catalyzed the discovery of a wide range of phenomena [25, 33], including superconductivity [23, 34–36], anomalous and fractional Hall effects [37–45], Wigner crystallization [46–49], quasicrystalline behavior [50–54], and correlated states [22, 55–62]. However, these remarkable phenomena often occur at specific twist angles, and additionally suffer from twist-angle disorder [63–65]. Moreover, synthetic platforms like photonic crystals or ultracold atoms cannot be easily twisted. The successes—but also the limitations—of moiré heterostructures therefore motivate the search for new ways to optimize the quantum geometric tensor in solid-state and synthetic matter via real-space geometry.

Here we show that a newly discovered family of aperiodic tilings [66, 67] offers a real-space geometric pathway to tune the quantum geometric tensor. This is the only family of aperiodic tilings parametrically connected by a single real parameter ℓ [68]. This parameter determines

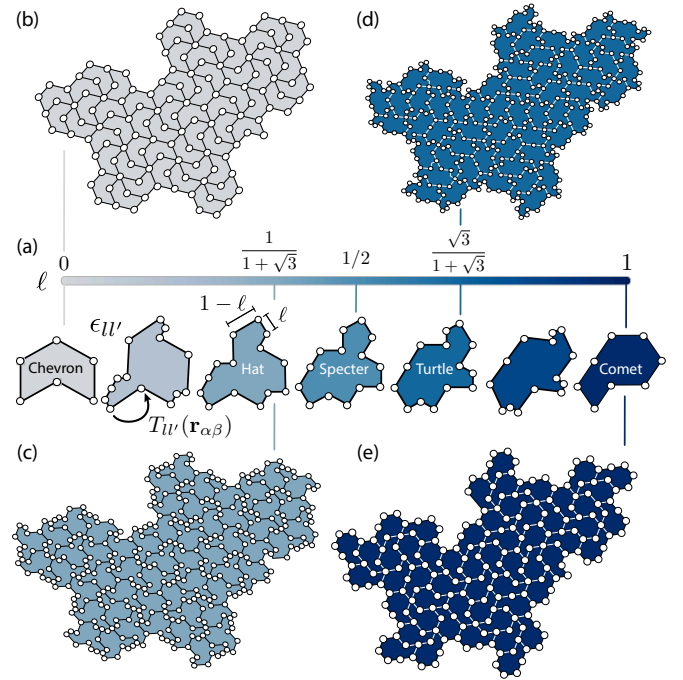


Figure 1. Tiles and tilings for different values of the tile side length, defined by two side lengths, ℓ and $1 - \ell$. (a) shows a selection of tiles, including the Chevron, Hat, Turtle, and Comet. Their corresponding aperiodic tilings are shown in (b–e). For each ℓ we place two orbitals l at every vertex, with onsite terms $\epsilon_{ll'}$. Pairs of sites $\{\alpha, \beta\}$ are connected by the space and orbital dependent hopping $T_{ll'}(\mathbf{r}_{\alpha\beta})$, see Eq. (1).

the position of all atomic sites while preserving the quasicrystalline long-range order. Allowing the hoppings to depend on atomic positions, we show that changes in ℓ translate into changes of the quantum geometric tensor [29, 32, 69], expressed in terms of a real-space Chern marker [70] and quantum metric [71, 72]. Changes in the real-space Chern marker induced by ℓ induce phase transitions in and out of a topological phase, which exists in an expanded parameter space compared to the same model in

crystals. The parameter ℓ also tunes the trace of the quantum metric [26–30], which contributes to the superfluid stiffness and kinetic inductance [25, 73–77], enters optical sum rules [78–80], and determines localization [81] and entanglement properties [82]. Hence, changing the real-space geometry using ℓ allows one to tune the quantum geometric tensor.

Geometric control of topology—Fig. 1a shows the Hat family of aperiodic tilings, parameterized by a real number $\ell \in [0, 1]$. It parametrizes the two independent lengths of parallel sides, $a = \ell$ and $b = 1 - \ell$. By tuning ℓ , one can continuously interpolate between different tiles in the family. The Hat tiling [$\ell = 1/(1 + \sqrt{3})$] made headlines as the first aperiodic monotile [66, 67]. Other named tiles are the *Specter* [$\ell = 1/2$], the *Turtle* [$\ell = \sqrt{3}/(1 + \sqrt{3})$], the *Chevron* [$\ell = 0$], and the *Comet* [$\ell = 1$] which sets our unit of length. Previous work has shown that a non-bipartite version of the Hat tiling shares similar electron properties with those of graphene [84] when all the hoppings are set to be equal. Here, we focus on the bipartite version of these tilings, and describe their construction in Appendix A of the Supplemental Material (SM) [85], by adapting the code published along with Ref. [86].

To exemplify how ℓ can control the electronic quantum geometry we consider a non-crystalline generalization of the Qi-Wu-Zhang Chern insulator model [87] on the vertices of the tiling, see Fig. 1a-e, that reads [88–91]:

$$\begin{aligned} \mathcal{H} = & \sum_{\langle\alpha,\beta\rangle} \sum_{l,l' \in \{1,2\}} T_{ll'}(r_{\alpha\beta}, \theta_{\alpha\beta}) c_{\alpha,l}^\dagger c_{\beta,l'} \\ & + \sum_{\alpha} \sum_{l,l' \in \{1,2\}} \epsilon_{ll'} c_{\alpha,l}^\dagger c_{\alpha,l'}. \end{aligned} \quad (1)$$

The hopping amplitude between two orbitals l and l' at sites α and β sharing an edge, $T_{ll'}(r_{\alpha\beta}, \theta_{\alpha\beta})$, depends on the inter-atomic separation $r_{\alpha\beta} = |\mathbf{r}_\alpha - \mathbf{r}_\beta|$ and the polar angle $\theta_{\alpha\beta}$. We choose the hopping to be $T(r_{\alpha\beta}, \theta_{\alpha\beta}) = h(\theta_{\alpha\beta})f(r_{\alpha\beta})$, with $f(r_{\alpha\beta}) = \exp(1 - r_{\alpha\beta}/\bar{a})$ and $h(\theta_{\alpha\beta}) = -(1/2)\sigma_z - (it/2)[\cos(\theta_{\alpha\beta})\sigma_x + \sin(\theta_{\alpha\beta})\sigma_y]$, and the onsite energy as $\epsilon = (2 + M)\sigma_z$. Here \bar{a} denotes the average bond-length and $(\sigma_x, \sigma_y, \sigma_z)$ are the Pauli matrices acting in orbital space. If we would choose α, β to lie on a square lattice we would recover the crystalline Chern insulator of Ref. [87].

The corresponding bulk energy spectrum is shown in Fig. 2a as a function of ℓ . It is symmetric with respect to zero energy as a consequence of a chiral symmetry [90] that places the model in class D of the Altland-Zirnbauer classification [92]. This feature is not essential to our findings. At the extreme values $\ell \approx 0, 1$ the spectrum is gapped and we expect the bands to be topologically trivial. The reason is that at these values of ℓ many sites come together in real space, forming clusters of sites (see Fig. 1a and Supplemental Video). The exponential form of $f(r_{\alpha\beta})$ leads to a strong suppression of the hoppings between clusters, exponentially localizing the wave-functions to these

clusters. Since exponentially localized wave-functions are topologically trivial, so the gaps are all trivial [93–95].

This expectation is confirmed by computing the bulk average of the local-Chern marker [96]

$$C_{\mathbf{r}_\alpha} = 2\pi \text{Im} \sum_l \langle \mathbf{r}_\alpha, l | \hat{P} [\hat{Q}\hat{X}, \hat{P}\hat{Y}] \hat{P} | \mathbf{r}_\alpha, l \rangle, \quad (2)$$

where $\hat{P} = \sum_{E < E_F} |E\rangle\langle E|$ is the projector onto occupied eigenstates states $|E\rangle$ below the Fermi energy E_F , $\hat{Q} = 1 - \hat{P}$, and \hat{X} and \hat{Y} the position operators in the plane. Its average over a bulk real-space region of area \mathcal{A}_b (see Appendix C in SM [85]), $C = (1/\mathcal{A}_b) \sum_{\alpha \in \text{Bulk}} C_{\mathbf{r}_\alpha}$, determines the bulk Chern number, C , which is approximately quantized if the occupied states are topological [70]. We find that the average of the local-Chern marker is zero when we place E_F within any of the gaps seen at $\ell \approx 0, 1$, as advertised.

As we tune ℓ , the angle- and position-dependence of the hoppings in Eq. (1) allows the spectrum to evolve, see Fig. 2a. At $\ell \approx 0.28$ we observe band closings, suggesting a topological phase transition.

Topological transitions would imply the appearance of in-gap spectral weight corresponding to topological edge states in the total momentum-resolved density of states, or spectral function. We define the spectral function by projecting the real-space Hamiltonian \mathcal{H} onto plane-wave states, $A(E, \mathbf{p}) = \sum_l \langle \mathbf{p}, l | \delta(\mathcal{H} - E) | \mathbf{p}, l \rangle$, where $|\mathbf{p}, l\rangle = \sum_\alpha e^{i\mathbf{p}\mathbf{r}_\alpha} |\mathbf{r}_\alpha, l\rangle$, see Appendix B in SM [85]. This function is measurable in angle-resolved photoemission spectroscopy even without translational invariance [97–102]. Note that, unlike the crystalline case, the components of \mathbf{p} are not restricted to the interval $[0, 2\pi]$. Comparing Figs. 2b and c, at either side of the gap closing (with $\ell = 0.23$ and $\ell = 0.33$, respectively) we see the appearance of in-gap spectral weight, as expected for a topological transition (see also Supplemental Video).

We confirm the topological nature of the in-gap states at $\ell = 0.33$ by computing the local Chern marker at $E_F = -1.15$, see Fig. 2d. For these parameters its bulk average is $C \approx 0.98$, confirming the topological phase. These results show that we can tune the topological phase by varying ℓ while keeping the filling fixed. For example, at $E_F = -1.15$ (dashed line in Fig. 2c), a trivial aperiodic tiling leads to an aperiodic tiling with finite Chern number.

We now ask, how far do the topological properties survive in parameter space, compared to the crystalline lattice model with the same Hamiltonian parameters? Because the bulk average of the local Chern marker is only approximately quantized, it is more convenient to answer this question with a local marker that is exactly an integer in the bulk. Such a marker can be obtained using the spectral localizer [103–106]

$$\mathcal{L} = (\hat{\mathcal{H}} - E_0 \mathbb{1}) \sigma_z + \kappa \left[(\hat{X} - x_0 \mathbb{1}) \sigma_x + (\hat{Y} - y_0 \mathbb{1}) \sigma_y \right], \quad (3)$$

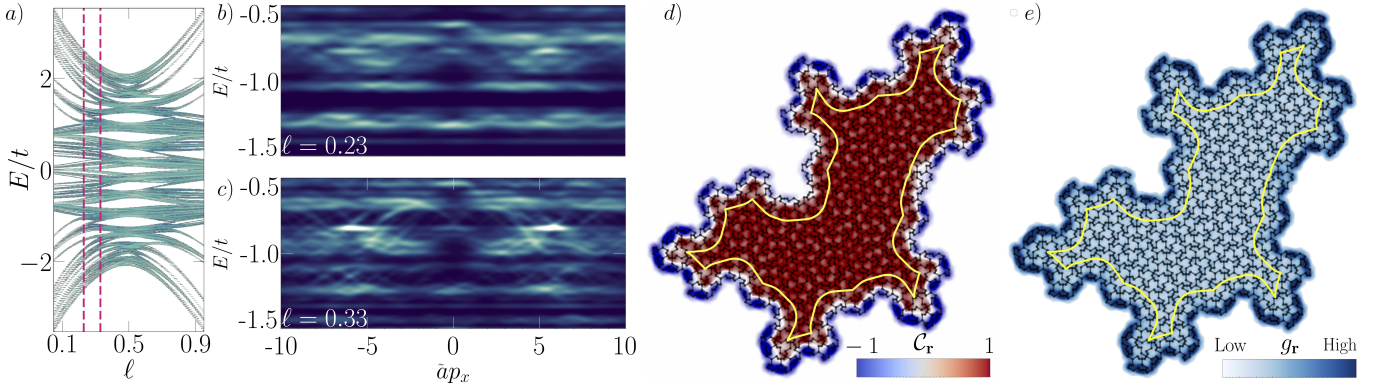


Figure 2. Spectral and topological properties of the model for different parameter values ℓ . (a) Energy spectrum of the bulk Hamiltonian as a function of the parameter ℓ . We obtain the bulk spectrum by excluding states whose weight inside the yellow contour in (d) and (e) is smaller than their weight outside it. Magenta dashed lines indicate the ℓ values used in panels (b) and (c). The yellow dashed line indicates the Fermi energy E_F . (b) Spectral function $\mathcal{A}(E, \mathbf{p})$ for $\ell = 0.23$, showing a full gap at the energy indicated by the white dashed line. (c) Spectral function $\mathcal{A}(E, \mathbf{p})$ for $\ell = 1/3$, showing the presence of edge states within bulk gaps. (d) Local Chern marker $C_{\mathbf{r}_i}$ Eq. (2), evaluated at the energy indicated by the white dashed line in (c) for $\ell = 1/3$. The yellow solid line outlines the bulk region used to perform the averaging. In this region, the average value of the local Chern marker is 0.98. (e) Local quantum metric g_r , Eq. (5), computed at the E_F indicated by the dashed line in (c) for $\ell = 1/3$. We observe that the local quantum metric takes large values at the edges, indicating delocalized edge states. In all the panels the system has 2530 sites and $M/t = -2.7$. In panels (b) and (c) we used the kernel polynomial method [83] to compute the spectral function with 512 moments.

where E_0 is the reference energy at which we want to probe topology and x_0 and y_0 are chosen in the bulk of the system [107]. The scalar κ is fixed to compensate the differences in scales between $\hat{\mathcal{H}}$ and the position operators \hat{X} , and \hat{Y} , see Appendix D in SM [85]. The half-signature of the localizer, $\frac{1}{2}\text{Sig}(\mathcal{L})$, defined as the half-difference between the number of positive and negative eigenvalues, is an integer that equals the bulk Chern number [103–106]. In turn, the minimal eigenvalue of the spectral localizer, the localizer gap, determines the stability of a given phase, since a topological phase transition can only occur if the localizer gap closes [106], see Appendix D in SM [85].

As a reference, when applied on a square lattice, the model defined in Eq. (1) only has topological phases when $0 < M/t < -4$. In contrast, we see in Fig. 3a that the phase diagram of the Hat family as a function of ℓ and M/t extends further. The topological bands survive for much larger values of M/t compared to the square lattice model, delimited by the dashed lines in Fig. 3a, especially around $\ell \approx 0.5$. Consistently, we see that the localizer gap, shown in Fig. 3b, closes at the phase boundaries.

Given that ℓ serves as a tuning parameter for inducing topological phase transitions, one might ask whether it can also be used to control a disordered induced Anderson transition. To address this question, we introduce a random onsite potential

$$V = \sum_{\alpha} \sum_{ll'} V_{\alpha, ll'} c_{\alpha, l}^\dagger c_{\alpha, l'}, \quad (4)$$

where $V_{\alpha, ll'} = V_0 \delta_{ll'}$ represent a site-dependent potential drawn from a uniform distribution in the range

$[-W/2, W/2]$, where W controls the disorder strength. We observe in Fig. 3b that the system remains topological for values of $W/t \leq 1$ before undergoing an Anderson transition, signaled by the closing of the average localizer gap, shown in Fig. 3d. As in crystals, for specific values of ℓ , such as $\ell = 0.8$, we observe that the system, initially trivial in the clean limit, transitions into a topological phase as W increases, realizing a topological Anderson insulator [108–110]. Interestingly, ℓ can be used as an additional knob to control a topological Anderson transition at fixed disorder strength, a mechanism specific to this tiling family.

Geometric control of the quantum metric—The local Chern marker is the imaginary part of a more general tensor called the quantum geometric tensor [26–32], which can also be controlled by tuning ℓ . Its real part is known as the quantum metric [29, 31, 32], and is proportional to the real-space spread of occupied states. By expressing it as a local real-space quantity (see Appendix C in SM [85] and Refs. [71, 72])

$$\mathbf{g}_{\mathbf{r}_\alpha} = 2\pi \text{Re} \sum_{\mu=\{x,y\}} \sum_l \langle \mathbf{r}_\alpha, l | \hat{P} \hat{r}_\mu \hat{Q} \hat{r}_\mu \hat{P} | \mathbf{r}_\alpha, l \rangle, \quad (5)$$

where $\hat{r}_x = \hat{X}$ and $\hat{r}_y = \hat{Y}$, we can use it to observe edge-state signatures, as shown in Fig. 2e for the topological state at $\ell = 0.33$ at $E_F = -1.15$. We see $g_{\mathbf{r}_\alpha}$ reaches its maximum values at the edges of the system, as expected for delocalized topological edge states.

As with the bulk local Chern marker, the bulk quantum metric, is also tunable as a function of the parameter ℓ at a given filling. We define the bulk quantum

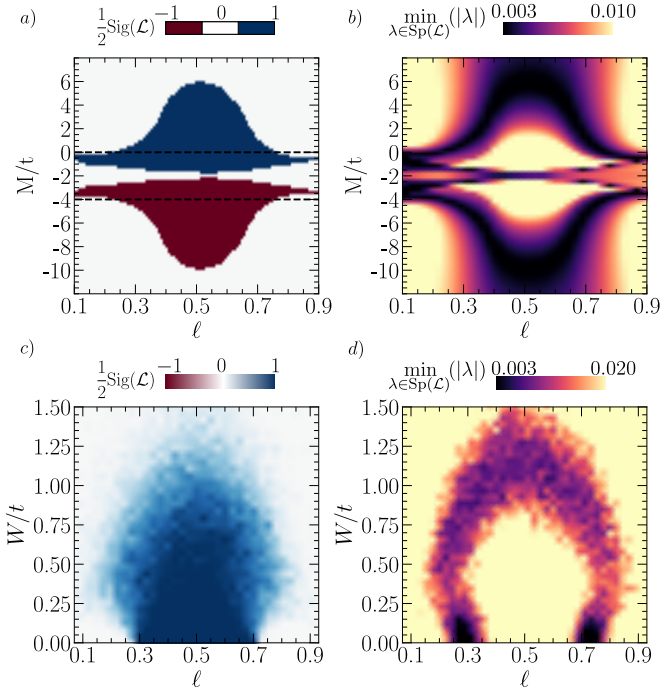


Figure 3. Topological phase diagram. (a) Bulk half-signature of the spectral localizer at $E_0 = E_F$ as a function of both the geometrical parameter ℓ and the value of the onsite term M/t . E_F is fixed at 3/4 filling out of a total of $N_{\text{sites}} \times N_{\text{orbs}} = 2530 \times 2$ states. We observe topological phases for a wider parameter region compared to the square-lattice crystalline model, whose phase boundaries are delimited by the black dashed lines. (b) Localizer gap corresponding to (a). The gap in the spectrum of the spectral localizer closes at the boundary between the topological and trivial phases of panel (a). (c) Bulk half-signature of the spectral localizer averaged over 50 disorder realizations at $E_0 = E_F$ and $M/t = 0.5$, as a function of ℓ and onsite disorder strength W/t . We observe two types of behavior as we increase W/t for fixed ℓ : either the clean system is topological and transitions into a trivial Anderson insulator (e.g. at $\ell = 0.5$), or a trivial clean system transitions into a topological Anderson insulator, to later become a trivial Anderson insulator (e.g. at $\ell = 0.8$ or $\ell = 0.2$). (d) The localizer gap vanishes at the interface between the topological and trivial Anderson insulators in (c). In all panels, the system has $N_{\text{sites}} = 2530$ sites and $\kappa = 0.01$.

metric by averaging Eq. (5) over a real-space region of area \mathcal{A}_b as $G = (1/\mathcal{A}_b) \sum_{\alpha \in \text{Bulk}} g_{\alpha}$, see Appendix C in SM [85]. Tuning G is desirable in several contexts. For instance, G is known to be bounded from below by the Chern number, $G \geq C$, an inequality known as the trace inequality [111–116]. When a band saturates this inequality it is termed vortexable or ideal [115, 116], as it is a favorable starting point to realize fractional Chern insulator states [117–119]. The quantum metric enters the superfluid stiffness [25, 73–77] and optical sum rules bounding topological gaps [78–80, 111]. The quantum metric depends on the real-space position, or embedding, of the orbitals [31, 120–126], controlled by ℓ in our

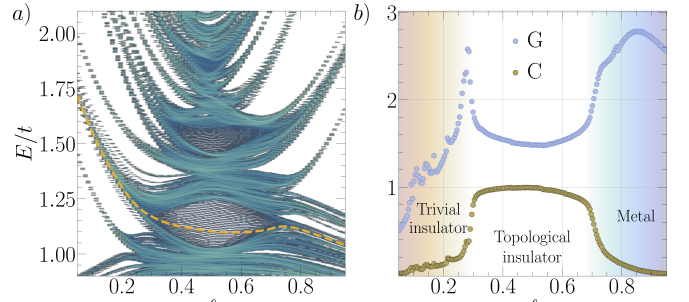


Figure 4. (a) Energy spectrum as a function of ℓ , showing a zoomed-in version of Fig. 1a including bulk and edge states. 3/4 filling is shown as a yellow dashed line in (a). (b) Bulk trace of the local quantum metric G and local Chern marker C for this filling as a function of ℓ . At small ℓ the sites cluster and localize the wave-functions for this filling, leading to a small G with $C \approx 0$. At intermediate $\ell \approx 0.5$, $G \geq C \approx 1$, satisfying the trace inequality. For large $\ell \gtrsim 0.7$ this filling sits in the middle of a band of delocalized states with increased G . In both panels, the system has $N_{\text{sites}} = 2530$ and $M/t = -2.7$.

system. In crystals, the embedding-dependence can be exploited to optimize responses such as the photovoltaic efficiency [124].

Fig. 4 shows the tunability of the quantum geometric tensor by plotting the trace of the local Chern marker C and the local quantum metric G as a function of ℓ . For 3/4 filling (dashed yellow line in Fig. 4a) G decreases as ℓ decreases with $C \approx 0$, see Fig. 4b. This is consistent with the fact that for these parameters the bands are narrow, topologically trivial, and states are localized due to the clustering of sites (see Supplemental Video). In contrast, at intermediate values of $\ell \approx 0.5$ the local Chern marker is approximately quantized to $C \approx 1$. The quantum metric decreases but does not saturate the trace inequality $G \geq C$, as seen in other Chern insulator models [127, 128]. At large $\ell \gtrsim 0.7$, C decreases to zero while G increases. This indicates that the states at this filling are more delocalized, consistent with the fact that E_F falls within a trivial band with a relatively large spread in energy, see Fig. 4a.

Conclusions—In this work we have used the real-space geometric parameter ℓ , which continuously connects members of the Hat family of aperiodic tilings, to tune the quantum geometric tensor. The parametrization in terms of ℓ is unique to this family, offering a new knob to control transport properties of aperiodic tilings. By allowing the hopping amplitudes to depend on the relative positions of the atoms, we have shown that ℓ controls the transition between trivial and topological phases, also in the presence of disorder. The parameter space supporting topological phases is broader than that of the square-lattice counterpart, highlighting the enhanced tunability offered by these tilings.

We have shown how ℓ tunes the quantum metric, which

underlies key physical properties such as the superfluid stiffness [25, 73–77, 129] and the optical weight [79, 130–132]. The ability to tune the quantum metric suggests avenues to engineer properties of unconventional superconductors [133], photonic systems [134, 135], and correlated electron systems [136–139].

The continuously parametrization in terms of ℓ can be exploited in different physical contexts. The systems we consider here could be realized in electronic systems by lithographic patterning of solid-state systems [140], depositing CO molecules on metals [141, 142], or by engineering 2D Shiba states with magnetic ad-atoms on superconductors [143–145]. Moiré heterostructures have also been used to realize unconventional tessellations [146]. Choosing different ℓ provides a new tuning knob to design topology and geometry in photonic metamaterials [6, 147–150], polaritonic systems [151], electrical circuits [152], microwave networks [153], acoustic [154] and mechanical [155–157] metamaterials. More broadly, the tunability of this family of aperiodic tilings has already proven useful in enhancing earthquake detection [86] and could benefit other areas such the study of spin models [158], elasticity [159, 160], and fluids [161] on aperiodic tilings.

Acknowledgments — We thank E. Ben Achour, P. D’Ornellas, F. Flicker, L. Gómez Paz, Q. Marsal, S. Pachhal, M. Thumin, D. Varjas, and M. Yoshii for useful discussions and suggestions. We are grateful to P. D’Ornellas and S. Roche for their critical reading of the manuscript. J. S. is supported by the program QuanTEdu-France n° ANR-22-CMAS-0001 France 2030. A. G. G. is supported by the European Research Council (ERC) Consolidator grant under grant agreement No. 101042707 (TOPO-MORPH).

-
- * hector.roche@neel.cnrs.fr
- † justin.schirmann@neel.cnrs.fr
- ‡ aurmo@geus.dk
- § adolfo.grushin@neel.cnrs.fr
- [1] C. Janot, *Quasicrystals - A Primer* (Clarendon Press Oxford, 1992).
- [2] Z. Stadnik, *Physical Properties of Quasicrystals* (Springer Series in Solid-State Sciences, 1999).
- [3] T. Janssen, G. Chapuis, and M. d. Boissieu, *Aperiodic Crystals From Modulated Phases to Quasicrystals*, Acta Crystallographica Section A, Vol. 74 (Oxford University Press, 2018).
- [4] R. Penrose, “The role of aesthetics in pure and applied mathematical research”, Bulletin of the Institute of Mathematics and its Applications **10**, 266ff (1974).
- [5] G. Shephard, R. Ammann, and B. Grünbaum, Aperiodic tiles., *Discrete and computational geometry* **8**, 1 (1992).
- [6] Y. E. Kraus, Y. Lahini, Z. Ringel, M. Verbin, and O. Zilbermanberg, Topological States and Adiabatic Pumping in Quasicrystals, *Phys. Rev. Lett.* **109**, 106402 (2012).
- [7] D. T. Tran, A. Dauphin, N. Goldman, and P. Gaspard, Topological Hofstadter insulators in a two-dimensional quasicrystal, *Phys. Rev. B* **91**, 085125 (2015).
- [8] M. A. Bandres, M. C. Rechtsman, and M. Segev, Topological Photonic Quasicrystals: Fractal Topological Spectrum and Protected Transport, *Physical Review X* **6**, 011016 (2016).
- [9] J.-N. Fuchs and J. Vidal, Hofstadter butterfly of a quasicrystal, *Phys. Rev. B* **94**, 205437 (2016).
- [10] H. Huang and F. Liu, Theory of spin Bott index for quantum spin Hall states in nonperiodic systems, *Phys. Rev. B* **98**, 125130 (2018).
- [11] H. Huang and F. Liu, Theory of spin Bott index for quantum spin Hall states in nonperiodic systems, *Physical Review B* **98**, 125130 (2018).
- [12] J.-N. Fuchs, R. Mosseri, and J. Vidal, Landau levels in quasicrystals, *Phys. Rev. B* **98**, 145 (2018).
- [13] T. A. Loring, Bulk spectrum and K-theory for infinite-area topological quasicrystals, *Journal of Mathematical Physics* **60**, 081903 (2019).
- [14] D. Varjas, A. Lau, K. Pöyhönen, A. R. Akhmerov, D. I. Pikulin, and I. C. Fulga, Topological Phases without Crystalline Counterparts, *Phys. Rev. Lett.* **123**, 196401 (2019).
- [15] R. Chen, D.-H. Xu, and B. Zhou, Topological anderson insulator phase in a quasicrystal lattice, *Phys. Rev. B* **100**, 115311 (2019).
- [16] A.-L. He, L.-R. Ding, Y. Zhou, Y.-F. Wang, and C.-D. Gong, Quasicrystalline Chern insulators, *Phys. Rev. B* **100**, 214109 (2019).
- [17] C. W. Duncan, S. Manna, and A. E. B. Nielsen, Topological models in rotationally symmetric quasicrystals, *Phys. Rev. B* **101**, 115413 (2020).
- [18] O. Zilbermanberg, Topology in quasicrystals, *Opt. Mater. Express* **11**, 1143 (2021).
- [19] C.-B. Hua, Z.-R. Liu, T. Peng, R. Chen, D.-H. Xu, and B. Zhou, Disorder-induced chiral and helical Majorana edge modes in a two-dimensional Ammann-Beenker quasicrystal, *Phys. Rev. B* **104**, 155304 (2021).
- [20] J. Jeon, M. J. Park, and S. Lee, Length scale formation in the Landau levels of quasicrystals, *Phys. Rev. B* **105**, 045146 (2022).
- [21] J. Schirmann, S. Franca, F. Flicker, and A. G. Grushin, Physical properties of an aperiodic monolite with graphene-like features, chirality, and zero modes, *Phys. Rev. Lett.* **132**, 086402 (2024).
- [22] Y. Cao, V. Fatemi, A. Demir, S. Fang, S. L. Tomarken, J. Y. Luo, J. D. Sanchez-Yamagishi, K. Watanabe, T. Taniguchi, E. Kaxiras, R. C. Ashoori, and P. Jarillo-Herrero, Correlated insulator behaviour at half-filling in magic-angle graphene superlattices, *Nature* **556**, 80 (2018).
- [23] Y. Cao, V. Fatemi, S. Fang, K. Watanabe, T. Taniguchi, E. Kaxiras, and P. Jarillo-Herrero, Unconventional superconductivity in magic-angle graphene superlattices, *Nature* **556**, 43 (2018).
- [24] E. Y. Andrei and A. H. MacDonald, Graphene bilayers with a twist, *Nature Materials* **19**, 1265 (2020).
- [25] P. Törmä, S. Peotta, and B. A. Bernevig, Superconductivity, superfluidity and quantum geometry in twisted multilayer systems, *Nature Reviews Physics* **4**, 528–542 (2022).
- [26] G. Fubini, On a Metric defined by a Hermitian form, *Atti Inst. Veneto Sci. Lett. Arti* **63**, 501 (1904).
- [27] E. Study, Kürzeste wege im komplexen gebiet, *Mathematische Annalen* **60**, 321 (1905).

- [28] R. Cheng, Quantum Geometric Tensor (Fubini-Study Metric) in Simple Quantum System: A pedagogical Introduction, Preprint at <https://arxiv.org/abs/1012.1337> (2013).
- [29] J. Yu, B. A. Bernevig, R. Queiroz, E. Rossi, P. Törmä, and B.-J. Yang, Quantum geometry in quantum materials, Preprint at <https://arxiv.org/abs/2501.00098> (2024).
- [30] T. Liu, X.-B. Qiang, H.-Z. Lu, and X. C. Xie, Quantum geometry in condensed matter, *National Science Review* **12**, nwae334 (2024).
- [31] P. Törmä, Essay: Where can quantum geometry lead us?, *Phys. Rev. Lett.* **131**, 240001 (2023).
- [32] N. Verma, P. J. W. Moll, T. Holder, and R. Queiroz, Quantum geometry: Revisiting electronic scales in quantum matter, Preprint at <https://arxiv.org/abs/2504.07173> (2025).
- [33] D. M. Kennes, M. Claassen, L. Xian, A. Georges, A. J. Millis, J. Hone, C. R. Dean, D. N. Basov, A. N. Pasupathy, and A. Rubio, Moiréheterostructures as a condensed-matter quantum simulator, *Nature Physics* **17**, 155 (2021).
- [34] M. Yankowitz, S. Chen, H. Polshyn, Y. Zhang, K. Watanabe, T. Taniguchi, D. Graf, A. F. Young, and C. R. Dean, Tuning superconductivity in twisted bilayer graphene, *Science* **363**, 1059 (2019).
- [35] G. Chen, A. L. Sharpe, P. Gallagher, I. T. Rosen, E. J. Fox, L. Jiang, B. Lyu, H. Li, K. Watanabe, T. Taniguchi, J. Jung, Z. Shi, D. Goldhaber-Gordon, Y. Zhang, and F. Wang, Signatures of tunable superconductivity in a trilayer graphene moirésuperlattice, *Nature* **572**, 215 (2019).
- [36] X. Lu, P. Stepanov, W. Yang, M. Xie, M. A. Aamir, I. Das, C. Urgell, K. Watanabe, T. Taniguchi, G. Zhang, A. Bachtold, A. H. MacDonald, and D. K. Efetov, Superconductors, orbital magnets and correlated states in magic-angle bilayer graphene, *Nature* **574**, 653 (2019).
- [37] J. Cai, E. Anderson, C. Wang, X. Zhang, X. Liu, W. Holtzmann, Y. Zhang, F. Fan, T. Taniguchi, K. Watanabe, Y. Ran, T. Cao, L. Fu, D. Xiao, W. Yao, and X. Xu, Signatures of fractional quantum anomalous Hall states in twisted MoTe₂, *Nature* **622**, 63 (2023).
- [38] Y. Zeng, Z. Xia, K. Kang, J. Zhu, P. Knüppel, C. Vaswani, K. Watanabe, T. Taniguchi, K. F. Mak, and J. Shan, Thermodynamic evidence of fractional Chern insulator in moiréMoTe₂, *Nature* **622**, 69 (2023).
- [39] H. Park, J. Cai, E. Anderson, Y. Zhang, J. Zhu, X. Liu, C. Wang, W. Holtzmann, C. Hu, Z. Liu, T. Taniguchi, K. Watanabe, J.-H. Chu, T. Cao, L. Fu, W. Yao, C.-Z. Chang, D. Cobden, D. Xiao, and X. Xu, Observation of fractionally quantized anomalous Hall effect, *Nature* **622**, 74 (2023).
- [40] F. Xu, Z. Sun, T. Jia, C. Liu, C. Xu, C. Li, Y. Gu, K. Watanabe, T. Taniguchi, B. Tong, J. Jia, Z. Shi, S. Jiang, Y. Zhang, X. Liu, and T. Li, Observation of Integer and Fractional Quantum Anomalous Hall Effects in Twisted Bilayer MoTe₂, *Phys. Rev. X* **13**, 031037 (2023).
- [41] K. Kang, B. Shen, Y. Qiu, Y. Zeng, Z. Xia, K. Watanabe, T. Taniguchi, J. Shan, and K. F. Mak, Evidence of the fractional quantum spin hall effect in moirémote2, *Nature* **628**, 522 (2024).
- [42] Z. Lu, T. Han, Y. Yao, A. P. Reddy, J. Yang, J. Seo, K. Watanabe, T. Taniguchi, L. Fu, and L. Ju, Fractional quantum anomalous hall effect in multilayer graphene, *Nature* **626**, 759 (2024).
- [43] J. Xie, Z. Huo, X. Lu, Z. Feng, Z. Zhang, W. Wang, Q. Yang, K. Watanabe, T. Taniguchi, K. Liu, Z. Song, X. C. Xie, J. Liu, and X. Lu, Even- and Odd-denominator Fractional Quantum Anomalous Hall Effect in Graphene Moire Superlattices, Preprint at <https://arxiv.org/abs/2405.16944> (2024).
- [44] D. Waters, A. Okounkova, R. Su, B. Zhou, J. Yao, K. Watanabe, T. Taniguchi, X. Xu, Y.-H. Zhang, J. Folk, and M. Yankowitz, Interplay of electronic crystals with integer and fractional Chern insulators in moiré pentalayer graphene, Preprint at <https://arxiv.org/abs/2408.10133> (2024).
- [45] Z. Lu, T. Han, Y. Yao, J. Yang, J. Seo, L. Shi, S. Ye, K. Watanabe, T. Taniguchi, and L. Ju, Extended Quantum Anomalous Hall States in Graphene/hBN Moiré Superlattices, Preprint at <https://arxiv.org/abs/2408.10203> (2024).
- [46] E. C. Regan, D. Wang, C. Jin, M. I. Bakti Utama, B. Gao, X. Wei, S. Zhao, W. Zhao, Z. Zhang, K. Yumigeta, M. Blei, J. D. Carlström, K. Watanabe, T. Taniguchi, S. Tongay, M. Crommie, A. Zettl, and F. Wang, Mott and generalized Wigner crystal states in WSe₂/WS₂ moirésuperlattices, *Nature* **579**, 359 (2020).
- [47] Y. Xu, S. Liu, D. A. Rhodes, K. Watanabe, T. Taniguchi, J. Hone, V. Elser, K. F. Mak, and J. Shan, Correlated insulating states at fractional fillings of moirésuperlattices, *Nature* **587**, 214 (2020).
- [48] H. Li, S. Li, E. C. Regan, D. Wang, W. Zhao, S. Kahn, K. Yumigeta, M. Blei, T. Taniguchi, K. Watanabe, S. Tongay, A. Zettl, M. F. Crommie, and F. Wang, Imaging two-dimensional generalized wigner crystals, *Nature* **597**, 650 (2021).
- [49] H. Li, Z. Xiang, A. P. Reddy, T. Devakul, R. Sailus, R. Banerjee, T. Taniguchi, K. Watanabe, S. Tongay, A. Zettl, L. Fu, M. F. Crommie, and F. Wang, Wigner molecular crystals from multielectron moiré artificial atoms, *Science* **385**, 86 (2024).
- [50] S. J. Ahn, P. Moon, T.-H. Kim, H.-W. Kim, H.-C. Shin, E. H. Kim, H. W. Cha, S.-J. Kahng, P. Kim, M. Koshino, Y.-W. Son, C.-W. Yang, and J. R. Ahn, Dirac electrons in a dodecagonal graphene quasicrystal, *Science* **361**, 782 (2018).
- [51] A. Uri, S. C. de la Barrera, M. T. Randeria, D. Rodan-Legrain, T. Devakul, P. J. D. Crowley, N. Paul, K. Watanabe, T. Taniguchi, R. Lifshitz, L. Fu, R. C. Ashoori, and P. Jarillo-Herrero, Superconductivity and strong interactions in a tunable moiréquasicrystal, *Nature* **620**, 762 (2023).
- [52] X. Lai, D. Guerci, G. Li, K. Watanabe, T. Taniguchi, J. Wilson, J. H. Pixley, and E. Y. Andrei, Imaging Self-aligned Moiré Crystals and Quasicrystals in Magic-angle Bilayer Graphene on hBN Heterostructures, Preprint at <https://arxiv.org/abs/2311.07819> (2023).
- [53] C.-Y. Hao, Z. Zhan, P. A. Pantaleón, J.-Q. He, Y.-X. Zhao, K. Watanabe, T. Taniguchi, F. Guinea, and L. He, Robust flat bands in twisted trilayer graphene moiréquasicrystals, *Nature Communications* **15**, 8437 (2024).
- [54] P. Alcázar Guerrero, V.-H. Nguyen, A. W. Cummings, J.-C. Charlier, and S. Roche, Proximity Effects Between the Graphene Quasicrystal and Magic-Angle Twisted Bilayer Graphene, Preprint at <https://arxiv.org/abs/2502.17069>

- (2025).
- [55] Y. Choi, J. Kemmer, Y. Peng, A. Thomson, H. Arora, R. Polski, Y. Zhang, H. Ren, J. Alicea, G. Refael, F. von Oppen, K. Watanabe, T. Taniguchi, and S. Nadj-Perge, Electronic correlations in twisted bilayer graphene near the magic angle, *Nature Physics* **15**, 1174 (2019).
- [56] A. L. Sharpe, E. J. Fox, A. W. Barnard, J. Finney, K. Watanabe, T. Taniguchi, M. A. Kastner, and D. Goldhaber-Gordon, Emergent ferromagnetism near three-quarters filling in twisted bilayer graphene, *Science* **365**, 605 (2019).
- [57] H. Polshyn, M. Yankowitz, S. Chen, Y. Zhang, K. Watanabe, T. Taniguchi, C. R. Dean, and A. F. Young, Large linear-in-temperature resistivity in twisted bilayer graphene, *Nature Physics* **15**, 1011 (2019).
- [58] E. Codecido, Q. Wang, R. Koester, S. Che, H. Tian, R. Lv, S. Tran, K. Watanabe, T. Taniguchi, F. Zhang, M. Bockrath, and C. N. Lau, Correlated insulating and superconducting states in twisted bilayer graphene below the magic angle, *Science Advances* **5** (2019).
- [59] X. Liu, Z. Hao, E. Khalaf, J. Y. Lee, Y. Ronen, H. Yoo, D. Haei Najafabadi, K. Watanabe, T. Taniguchi, A. Vishwanath, and P. Kim, Tunable spin-polarized correlated states in twisted double bilayer graphene, *Nature* **583**, 221 (2020).
- [60] C. Shen, Y. Chu, Q. Wu, N. Li, S. Wang, Y. Zhao, J. Tang, J. Liu, J. Tian, K. Watanabe, T. Taniguchi, R. Yang, Z. Y. Meng, D. Shi, O. V. Yazyev, and G. Zhang, Correlated states in twisted double bilayer graphene, *Nature Physics* **16**, 520 (2020).
- [61] G. Chen, A. L. Sharpe, E. J. Fox, Y.-H. Zhang, S. Wang, L. Jiang, B. Lyu, H. Li, K. Watanabe, T. Taniguchi, Z. Shi, T. Senthil, D. Goldhaber-Gordon, Y. Zhang, and F. Wang, Tunable correlated chern insulator and ferromagnetism in a moirésuperlattice, *Nature* **579**, 56 (2020).
- [62] Y. Cao, D. Rodan-Legrain, O. Rubies-Bigorda, J. M. Park, K. Watanabe, T. Taniguchi, and P. Jarillo-Herrero, Tunable correlated states and spin-polarized phases in twisted bilayer–bilayer graphene, *Nature* **583**, 215 (2020).
- [63] G. Li, A. Luican, J. M. B. Lopes dos Santos, A. H. Castro Neto, A. Reina, J. Kong, and E. Y. Andrei, Observation of van hove singularities in twisted graphene layers, *Nature Physics* **6**, 109 (2010).
- [64] I. Brihuega, P. Mallet, H. González-Herrero, G. Trambly de Laissardière, M. M. Ugeda, L. Magaud, J. M. Gómez-Rodríguez, F. Ynduráin, and J.-Y. Veuillen, Unraveling the Intrinsic and Robust Nature of van Hove Singularities in Twisted Bilayer Graphene by Scanning Tunneling Microscopy and Theoretical Analysis, *Phys. Rev. Lett.* **109**, 196802 (2012).
- [65] A. Uri, S. Grover, Y. Cao, J. A. Crosse, K. Bagani, D. Rodan-Legrain, Y. Myasoedov, K. Watanabe, T. Taniguchi, P. Moon, M. Koshino, P. Jarillo-Herrero, and E. Zeldov, Mapping the twist-angle disorder and landau levels in magic-angle graphene, *Nature* **581**, 47 (2020).
- [66] D. Smith, J. S. Myers, C. S. Kaplan, and C. Goodman-Strauss, An aperiodic monotile, *Preprint at https://arxiv.org/abs/2303.10798* (2023).
- [67] D. Smith, J. S. Myers, C. S. Kaplan, and C. Goodman-Strauss, A chiral aperiodic monotile, *Preprint at https://arxiv.org/abs/2305.17743* (2023).
- [68] Aperiodic tilings can be generated by the cut and project method. By varying continuously the cut angle one might expect to realize a continuous family of aperiodic tilings. However, varying this angle continuously typically results in jumps when new tiles appear, see e.g. [this video](#). We thank F. Flicker for this remark.
- [69] A. Abouelkomsan, K. Yang, and E. J. Bergholtz, Quantum metric induced phases in moiré materials, *Phys. Rev. Res.* **5**, L012015 (2023).
- [70] R. Resta, The insulating state of matter: a geometrical theory, *The European Physical Journal B* **79**, 121 (2011).
- [71] N. Marzari and D. Vanderbilt, Maximally localized generalized wannier functions for composite energy bands, *Phys. Rev. B* **56**, 12847 (1997).
- [72] Q. Marsal and A. M. Black-Schaffer, Enhanced quantum metric due to vacancies in graphene, *Phys. Rev. Lett.* **133**, 026002 (2024).
- [73] A. Julku, S. Peotta, T. I. Vanhala, D.-H. Kim, and P. Törmä, Geometric Origin of Superfluidity in the Lieb-Lattice Flat Band, *Phys. Rev. Lett.* **117**, 045303 (2016).
- [74] M. Tovmasyan, S. Peotta, P. Törmä, and S. D. Huber, Effective theory and emergent SU(2) symmetry in the flat bands of attractive hubbard models, *Phys. Rev. B* **94**, 245149 (2016).
- [75] F. Xie, Z. Song, B. Lian, and B. A. Bernevig, Topology-Bounded Superfluid Weight in Twisted Bilayer Graphene, *Phys. Rev. Lett.* **124**, 167002 (2020).
- [76] J. Herzog-Arbeitman, V. Peri, F. Schindler, S. D. Huber, and B. A. Bernevig, Superfluid weight bounds from symmetry and quantum geometry in flat bands, *Phys. Rev. Lett.* **128**, 087002 (2022).
- [77] S. Peotta, K.-E. Huhtinen, and P. Törmä, Quantum geometry in superfluidity and superconductivity, *Preprint at https://arxiv.org/abs/2308.08248* (2023).
- [78] W.-X. Qiu and F. Wu, Quantum geometry probed by chiral excitonic optical response of chern insulators, *Preprint at https://arxiv.org/abs/2407.03317* (2024).
- [79] Y. Onishi and L. Fu, Fundamental Bound on Topological Gap, *Physical Review X* **14** (2024).
- [80] P. M. Chiu, Topological signatures of the optical bound on maximal berry curvature: Applications to two-dimensional time-reversal-symmetric insulators, *Preprint at https://arxiv.org/abs/2501.17671* (2025).
- [81] C. W. Chiu, T. Xiang, S. A. Chen, and K. T. Law, Disorder-induced delocalization in flat-band systems with quantum geometry, *Preprint at https://arxiv.org/abs/2412.19056* (2024).
- [82] N. Paul, Area-law entanglement from quantum geometry, *Phys. Rev. B* **109**, 085146 (2024).
- [83] A. Weiße, G. Wellein, A. Alvermann, and H. Fehske, The kernel polynomial method, *Reviews of Modern Physics* **78**, 275–306 (2006).
- [84] J. Schirmann, S. Franca, F. Flicker, and A. G. Grushin, Physical properties of an aperiodic monotile with graphene-like features, chirality, and zero modes, *Physical Review Letters* **132** (2024).
- [85] The Supplemental Material includes an introduction to the inflation rules to generate the tilings, a discussion on how we calculate the spectral function and the quantum geometric tensor, and a discussion on choosing the value of κ for the spectral localizer. It includes Refs. [29, 32, 66, 69, 70, 86, 96, 103–106, 162–169]. We also include a video showing the tiling and its corresponding spectral function as a function ℓ .

- [86] A. Mordret and A. G. Grushin, Beating the aliasing limit with aperiodic monotile arrays, *Phys. Rev. Appl.* **23**, 034021 (2025).
- [87] X.-L. Qi, Y.-S. Wu, and S.-C. Zhang, Topological quantization of the spin hall effect in two-dimensional paramagnetic semiconductors, *Phys. Rev. B* **74**, 085308 (2006).
- [88] B. A. Bernevig, T. L. Hughes, and S.-C. Zhang, Quantum Spin Hall Effect and Topological Phase Transition in HgTe Quantum Wells, *Science* **314**, 1757 (2006).
- [89] B. A. Bernevig, *Topological Insulators and Topological Superconductors* (Princeton University Press, Princeton, 2013).
- [90] A. Agarwala and V. B. Shenoy, Topological Insulators in Amorphous Systems, *Physical Review Letters* **118**, 236402 (2017).
- [91] Z.-R. Liu, C.-B. Hua, T. Peng, and B. Zhou, Chern insulator in a hyperbolic lattice, *Phys. Rev. B* **105**, 245301 (2022).
- [92] A. Altland and M. R. Zirnbauer, Nonstandard symmetry classes in mesoscopic normal-superconducting hybrid structures, *Phys. Rev. B* **55**, 1142 (1997).
- [93] G. Panati, Triviality of Bloch and Bloch–Dirac Bundles, *Annales Henri Poincaré* **8**, 995 (2007).
- [94] C. Brouder, G. Panati, M. Calandra, C. Mourougane, and N. Marzari, Exponential localization of wannier functions in insulators, *Phys. Rev. Lett.* **98**, 046402 (2007).
- [95] A. A. Soluyanov and D. Vanderbilt, Wannier representation of \mathbb{Z}_2 topological insulators, *Phys. Rev. B* **83**, 035108 (2011).
- [96] R. Bianco and R. Resta, Mapping topological order in coordinate space, *Phys. Rev. B* **84**, 241106 (2011).
- [97] Q. Marsal, D. Varjas, and A. G. Grushin, Obstructed insulators and flat bands in topological phase-change materials, *Phys. Rev. B* **107**, 045119 (2023).
- [98] P. Corbae, S. Ciocys, D. Varjas, E. Kennedy, S. Zeltmann, M. Molina-Ruiz, S. M. Griffin, C. Jozwiak, Z. Chen, L.-W. Wang, A. M. Minor, M. Scott, A. G. Grushin, A. Lanzara, and F. Hellman, Observation of spin-momentum locked surface states in amorphous Bi₂Se₃, *Nature Materials* **22**, 200 (2023).
- [99] S. T. Ciocys, Q. Marsal, P. Corbae, D. Varjas, E. Kennedy, M. Scott, F. Hellman, A. G. Grushin, and A. Lanzara, Establishing Coherent Momentum-Space Electronic States in Locally Ordered Materials, *Preprint at https://arxiv.org/abs/2302.05945* (2023).
- [100] E. Rotenberg, W. Theis, K. Horn, and P. Gille, Quasicrystalline valence bands in decagonal alnico, *Nature* **406**, 602 (2000).
- [101] E. Rotenberg, W. Theis, and K. Horn, Electronic structure investigations of quasicrystals, *Progress in Surface Science* **75**, 237 (2004).
- [102] V. A. Rogalev, O. Gröning, R. Widmer, J. H. Dil, F. Bisti, L. L. Lev, T. Schmitt, and V. N. Strocov, Fermi states and anisotropy of Brillouin zone scattering in the decagonal Al–Ni–Co quasicrystal, *Nature Communications* **6**, 8607 (2015).
- [103] T. A. Loring, K-theory and pseudospectra for topological insulators, *Annals of Physics* **356**, 383 (2015).
- [104] T. A. Loring, A guide to the bott index and localizer index, *Preprint at https://arxiv.org/abs/1907.11791* (2019).
- [105] A. Cerjan and T. A. Loring, Local invariants identify topology in metals and gapless systems, *Physical Review B* **106**, 064109 (2022).
- [106] A. Cerjan and T. A. Loring, Classifying photonic topology using the spectral localizer and numerical k-theory, *APL Photonics* **9** (2024).
- [107] In practice, we choose the coordinates x_0 and y_0 by computing the geometric mean of the vertex coordinates.
- [108] J. Li, R.-L. Chu, J. K. Jain, and S.-Q. Shen, Topological anderson insulator, *Phys. Rev. Lett.* **102**, 136806 (2009).
- [109] C. W. Groth, M. Wimmer, A. R. Akhmerov, J. Tworzydlo, and C. W. J. Beenakker, Theory of the Topological Anderson Insulator, *Physical Review Letters* **103**, 196805 (2009).
- [110] D. A. Khudaiberdiev, Z. D. Kvon, M. S. Ryzhkov, D. A. Kozlov, N. N. Mikhailov, and A. Pimenov, Two-dimensional topological Anderson insulator in a HgTe-based semimetal, *Preprint at https://arxiv.org/abs/2410.23564* (2024).
- [111] I. Souza, T. Wilkens, and R. M. Martin, Polarization and localization in insulators: Generating function approach, *Phys. Rev. B* **62**, 1666 (2000).
- [112] S. A. Parameswaran, R. Roy, and S. L. Sondhi, Fractional quantum Hall physics in topological flat bands, *Comptes Rendus. Physique* **14**, 816 (2013).
- [113] R. Roy, Band geometry of fractional topological insulators, *Phys. Rev. B* **90**, 165139 (2014).
- [114] M. Claassen, C. H. Lee, R. Thomale, X.-L. Qi, and T. P. Devereaux, Position-Momentum Duality and Fractional Quantum Hall Effect in Chern Insulators, *Phys. Rev. Lett.* **114**, 236802 (2015).
- [115] P. J. Ledwith, G. Tarnopolsky, E. Khalaf, and A. Vishwanath, Fractional Chern insulator states in twisted bilayer graphene: An analytical approach, *Phys. Rev. Res.* **2**, 023237 (2020).
- [116] J. Wang, J. Cano, A. J. Millis, Z. Liu, and B. Yang, Exact Landau Level Description of Geometry and Interaction in a Flatband, *Phys. Rev. Lett.* **127**, 246403 (2021).
- [117] Z. Liu, E. J. Bergholtz, H. Fan, and A. M. Läuchli, Fractional Chern Insulators in Topological Flat Bands with Higher Chern Number, *Phys. Rev. Lett.* **109**, 186805 (2012).
- [118] E. J. Bergholtz and Z. Liu, Topological flat band models and fractional Chern insulators, *International Journal of Modern Physics B* **27**, 1330017 (2013).
- [119] A. Abouelkomsan, Z. Liu, and E. J. Bergholtz, Particle-hole duality, emergent fermi liquids, and fractional chern insulators in moiré flatbands, *Phys. Rev. Lett.* **124**, 106803 (2020).
- [120] C. Bena and G. Montambaux, Remarks on the tight-binding model of graphene, *New Journal of Physics* **11**, 095003 (2009).
- [121] M. Fruchart, D. Carpentier, and K. Gawedzki, Parallel transport and band theory in crystals, *Europhysics Letters* **106**, 60002 (2014).
- [122] E. Dobardžić, M. Dimitrijević, and M. V. Milovanović, Generalized bloch theorem and topological characterization, *Phys. Rev. B* **91**, 125424 (2015).
- [123] L.-K. Lim, J.-N. Fuchs, and G. Montambaux, Geometry of bloch states probed by Stückelberg interferometry, *Phys. Rev. A* **92**, 063627 (2015).
- [124] A. M. Cook, B. M. Fregoso, F. de Juan, S. Coh, and J. E. Moore, Design principles for shift current photovoltaics, *Nature Communications* **8**, 14176 (2017).
- [125] S. H. Simon and M. S. Rudner, Contrasting lattice geometry dependent versus independent quantities: Ramification of the spectral localizer, *Phys. Rev. B* **106**, 064110 (2022).

- fications for berry curvature, energy gaps, and dynamics, *Phys. Rev. B* **102**, 165148 (2020).
- [126] K.-E. Huhtinen, J. Herzog-Arbeitman, A. Chew, B. A. Bernevig, and P. Törmä, Revisiting flat band superconductivity: Dependence on minimal quantum metric and band touchings, *Phys. Rev. B* **106**, 014518 (2022).
- [127] I. Komissarov, T. Holder, and R. Queiroz, The quantum geometric origin of capacitance in insulators, *Nature Communications* **15**, 4621 (2024).
- [128] J. M. Romeral, A. W. Cummings, and S. Roche, Scaling of the integrated quantum metric in disordered topological phases, *Phys. Rev. B* **111**, 134201 (2025).
- [129] M. Thumin and G. Bouzerar, Flat-band superconductivity in a system with a tunable quantum metric: The stub lattice, *Phys. Rev. B* **107**, 214508 (2023).
- [130] N. Verma, T. Hazra, and M. Randeria, Optical spectral weight, phase stiffness, and T_c bounds for trivial and topological flat band superconductors, *Proceedings of the National Academy of Sciences* **118** (2021).
- [131] B. Ghosh, Y. Onishi, S.-Y. Xu, H. Lin, L. Fu, and A. Bansil, Probing quantum geometry through optical conductivity and magnetic circular dichroism, *Preprint at <https://arxiv.org/abs/2401.09689>* (2024).
- [132] W. J. Jankowski, A. S. Morris, A. Bouhon, F. N. Ünal, and R.-J. Slager, Optical manifestations and bounds of topological euler class, *Phys. Rev. B* **111**, L081103 (2025).
- [133] G. Shavit and J. Alicea, Quantum geometric unconventional superconductivity, *Preprint at <https://arxiv.org/abs/2411.05071>* (2024).
- [134] O. Bleu, D. D. Solnyshkov, and G. Malpuech, Measuring the quantum geometric tensor in two-dimensional photonic and exciton-polariton systems, *Physical Review B* **97** (2018).
- [135] I. Petrides, J. B. Curtis, M. Wesson, A. Yacoby, and P. Narang, Probing electromagnetic nonreciprocity with quantum geometry of photonic states, *Preprint at <https://arxiv.org/abs/2310.16174>* (2023).
- [136] S. R. Hassan, R. Shankar, and A. Chakrabarti, Quantum geometry of correlated many-body states, *Physical Review B* **98** (2018).
- [137] W. Chen and G. von Gersdorff, Measurement of interaction-dressed berry curvature and quantum metric in solids by optical absorption, *Preprint at <https://arxiv.org/abs/2202.03494>* (2022).
- [138] T. Kashihara, Y. Michishita, and R. Peters, Quantum metric on the brillouin zone in correlated electron systems and its relation to topology for chern insulators, *Physical Review B* **107** (2023).
- [139] J.-X. Hu, S. A. Chen, and K. T. Law, Anomalous coherence length in superconductors with quantum metric, *Communications Physics* **8**, 20 (2025).
- [140] N. Lassaline, D. Thureja, T. Chervy, D. Petter, P. A. Murthy, A. W. Knoll, and D. J. Norris, Freeform electronic and photonic landscapes in hexagonal boron nitride, *Nano Letters* **21**, 8175 (2021).
- [141] K. K. Gomes, W. Mar, W. Ko, F. Guinea, and H. C. Manoharan, Designer Dirac fermions and topological phases in molecular graphene, *Nature* **483**, 306 (2012).
- [142] S. N. Kempkes, M. R. Slot, S. E. Freeney, S. J. M. Zevenhuizen, D. Vanmaekelbergh, I. Swart, and C. M. Smith, Design and characterization of electrons in a fractal geometry, *Nature Physics* **15**, 127 (2019).
- [143] S. Nadj-Perge, I. K. Drozdov, B. A. Bernevig, and A. Yazdani, Proposal for realizing Majorana fermions in chains of magnetic atoms on a superconductor, *Phys. Rev. B* **88**, 020407 (2013).
- [144] L. Schneider, P. Beck, J. Neuhaus-Steinmetz, L. Rózsa, T. Posske, J. Wiebe, and R. Wiesendanger, Precursors of Majorana modes and their length-dependent energy oscillations probed at both ends of atomic Shiba chains, *Nature Nanotechnology* **17**, 384 (2022).
- [145] M. O. Soldini, F. Küster, G. Wagner, S. Das, A. Aladarawsheh, R. Thomale, S. Lounis, S. S. P. Parkin, P. Sessi, and T. Neupert, Two-dimensional Shiba lattices as a possible platform for crystalline topological superconductivity, *Nature Physics* (2023).
- [146] D. Park, C. Park, K. Yananose, E. Ko, B. Kim, R. Engelke, X. Zhang, K. Davydov, M. Green, H.-M. Kim, S. H. Park, J. H. Lee, S.-G. Kim, H. Kim, K. Watanabe, T. Taniguchi, S. M. Yang, K. Wang, P. Kim, Y.-W. Son, and H. Yoo, Unconventional domain tessellations in moiré-of-moiré lattices, *Nature* (2025).
- [147] M. Notomi, H. Suzuki, T. Tamamura, and K. Edagawa, Lasing action due to the two-dimensional quasiperiodicity of photonic quasicrystals with a Penrose lattice, *Phys. Rev. Lett.* **92**, 123906 (2004).
- [148] L. Levi, M. Rechtsman, B. Freedman, T. Schwartz, O. Manela, and M. Segev, Disorder-Enhanced Transport in Photonic Quasicrystals, *Science* **332**, 1541 (2011).
- [149] M. A. Bandres, M. C. Rechtsman, and M. Segev, Topological photonic quasicrystals: Fractal topological spectrum and protected transport, *Phys. Rev. X* **6**, 011016 (2016).
- [150] T. Ozawa, H. M. Price, A. Amo, N. Goldman, M. Hafezi, L. Lu, M. C. Rechtsman, D. Schuster, J. Simon, O. Zilbermanberg, and I. Carusotto, Topological photonics, *Rev. Mod. Phys.* **91**, 015006 (2019).
- [151] D. Tanese, E. Gurevich, F. Baboux, T. Jacqmin, A. Lemaître, E. Galopin, I. Sagnes, A. Amo, J. Bloch, and E. Akkermans, Fractal energy spectrum of a polariton gas in a Fibonacci quasiperiodic potential, *Phys. Rev. Lett.* **112**, 146404 (2014).
- [152] A. Stegmaier, H. Brand, S. Imhof, A. Fritzsch, T. Helbig, T. Hofmann, I. Boettcher, M. Greiter, C. H. Lee, G. Bahl, A. Szameit, T. Kießling, R. Thomale, and L. K. Upreti, Realizing efficient topological temporal pumping in electrical circuits, *Preprint at <https://arxiv.org/abs/2306.15434>* (2023).
- [153] P. Vignolo, M. Bellec, J. Böhm, A. Camara, J.-M. Gambaudo, U. Kuhl, and F. Mortessagne, Energy landscape in a Penrose tiling, *Phys. Rev. B* **93**, 075141 (2016).
- [154] Y. Chen, M. Kadic, S. Guenneau, and M. Wegener, Isotropic chiral acoustic phonons in 3D quasicrystalline metamaterials, *Phys. Rev. Lett.* **124**, 235502 (2020).
- [155] C. He, X. Ni, H. Ge, X.-C. Sun, Y.-B. Chen, M.-H. Lu, X.-P. Liu, and Y.-F. Chen, Acoustic topological insulator and robust one-way sound transport, *Nature Physics* **12**, 1124 (2016).
- [156] Y. Ding, Y. Peng, Y. Zhu, X. Fan, J. Yang, B. Liang, X. Zhu, X. Wan, and J. Cheng, Experimental demonstration of acoustic chern insulators, *Phys. Rev. Lett.* **122**, 014302 (2019).
- [157] Y. Wang and O. Sigmund, Quasiperiodic mechanical metamaterials with extreme isotropic stiffness, *Extreme Mechanics Letters* **34**, 100596 (2020).
- [158] Y. Okabe, K. Niizeki, and Y. Araki, Ising model on the

- aperiodic smith hat, *Journal of Physics A: Mathematical and Theoretical* **57**, 125004 (2024).
- [159] R. Rieger and A. Danescu, Macroscopic elasticity of the hat aperiodic tiling, *Mechanics of Materials* **193**, 104988 (2024).
- [160] M. M. Naji and R. K. A. Al-Rub, Effective elastic properties of novel aperiodic monotile-based lattice metamaterials, *Materials & Design* **244**, 113102 (2024).
- [161] J. L. Plawsky, A. J. Rishty, and C. Woodcock, Transport through a chiral tiling: The effect of aperiodicity on flow and particle capture, *Chemical Engineering Science* **304**, 121020 (2025).
- [162] C. Kaplan, *An aperiodic monotile*.
- [163] J. P. Provost and G. Vallee, Riemannian structure on manifolds of quantum states, *Communications in Mathematical Physics* **76**, 289 (1980).
- [164] A. Marrazzo and R. Resta, Local theory of the insulating state, *Phys. Rev. Lett.* **122**, 166602 (2019).
- [165] G. L. Dirichlet, Über die reduction der positiven quadratischen formen mit drei unbestimmten ganzen zahlen., *Journal für die reine und angewandte Mathematik (Crelles Journal)* **1850**, 209 (1850).
- [166] G. Voronoi, Nouvelles applications des paramètres continus à la théorie des formes quadratiques. deuxième mémoire. recherches sur les paralléloèdres primitifs., *Journal für die reine und angewandte Mathematik (Crelles Journal)* **1908**, 198 (1908).
- [167] A. Cerjan, T. A. Loring, and H. Schulz-Baldes, Local markers for crystalline topology, *Phys. Rev. Lett.* **132**, 073803 (2024).
- [168] K. Y. Lee, S. Wong, S. Vaidya, T. A. Loring, and A. Cerjan, Classification of Fragile Topology Enabled by Matrix Homotopy, Preprint at <https://arxiv.org/abs/2503.03948> (2025).
- [169] H. Liu, C. Fulga, E. J. Bergholtz, and J. Asboth, Topological fine structure of an energy band, Preprint at <https://arxiv.org/abs/2312.08436>.

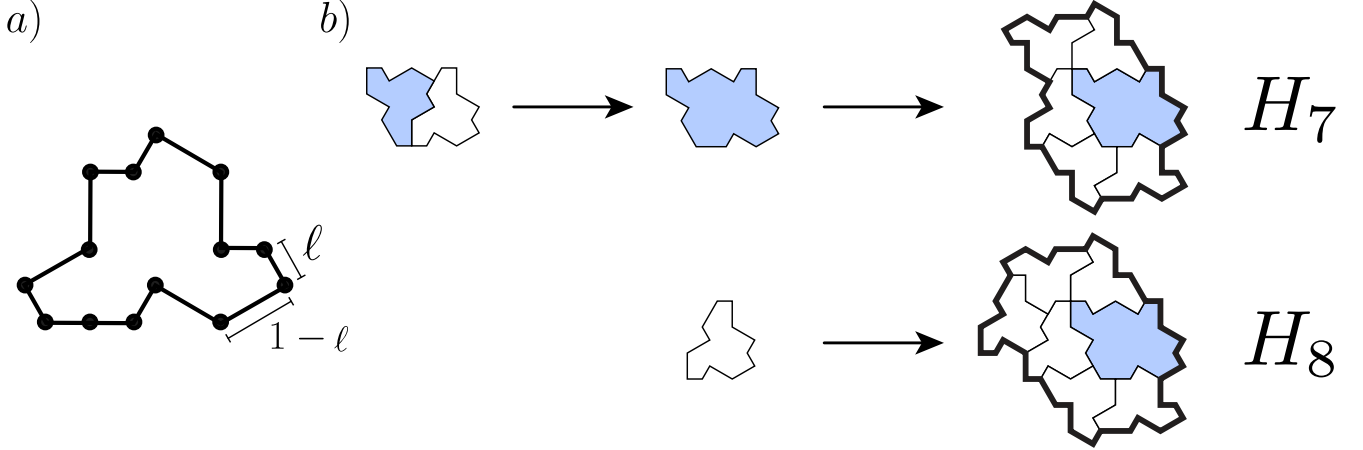


Figure S1. Tile and inflation rule. (a) A tile is a fourteen-sided polygon with edge lengths parameterized by a geometric parameter ℓ . In this example, the value of ℓ is taken to be $1/(1 + \sqrt{3})$. (b) To construct the tiling, we use clusters of tiles. We begin by defining a two-tile compound consisting of one tile (in white) and its mirror image (in pale blue). We then establish a substitution rule for both the single tile and the two-tile compound using the H_7 and H_8 clusters.

Supplementary Material for “A Family of Aperiodic Tilings with Tunable Quantum Geometric Tensor”

Appendix A: Generating aperiodic tilings from inflation rules

In this section, we describe the inflation procedure introduced in [66] and employed in [162] to generate the aperiodic tilings we use in the main text. As illustrated in Fig. S1, this procedure involves the successive replacement of one set of tiles with another made of a larger amount of tiles. In this work, we adapt the code used in Ref. [86] to generate the tilings presented in Figs. 1 and 2. We begin by examining a single tile, which is a 14-sided polygon whose edges can be grouped into pairs of equal-length, parallel segments, as shown in Fig. S1a. The first step is to combine one tile with its mirror image, forming a two-tile compound. Following [66], this two-tile compound can then be combined with six additional tiles to create a cluster, referred to as H_8 , or with five other tiles to form the H_7 cluster. The inflation process proceeds as follows: each individual tile is replaced by an H_8 cluster, while each two-tile compound is replaced by an H_7 cluster. This process can be iterated indefinitely to generate arbitrarily large lattices. The number of tiles after the n -th iteration is given by the following recursion relation

$$(H_7)_{n+1} = 5(H_8)_n + (H_7)_n, \quad (\text{A1})$$

$$(H_8)_{n+1} = 6(H_8)_n + (H_7)_n, \quad (\text{A2})$$

where $(H_7)_n$ (resp. $(H_8)_n$) denotes the number of tiles present in the H_7 (resp. H_8) cluster after the n -th iteration of the inflation procedure. In the main text we present results for the third iteration, which has 2530 sites. We have checked that our results are well converged with system size.

Appendix B: Bulk and surface spectral function.

In this Appendix we describe explicitly the procedure followed to compute the spectral function shown in Fig. 2. We first introduce the real space Green’s function. For a system composed of N_{sites} atoms and N_{orbs} internal degrees of freedom, the real-space Green’s function is an $N_{\text{sites}}N_{\text{orbs}} \times N_{\text{sites}}N_{\text{orbs}}$ matrix which reads

$$\mathcal{G}(E) = \lim_{\eta \rightarrow 0} (\mathcal{H} - (E - i\eta)\mathbf{1}_{N_{\text{sites}}N_{\text{orbs}}})^{-1}, \quad (\text{B1})$$

where \mathcal{H} is the real-space Hamiltonian and E is the energy at which the Green’s function is computed. In practice, η is taken to be finite. The value of η is related to the number of moments in the expansion in terms of Tchebychev’s polynomials used in the kernel polynomial method [83]. We now introduce the tight-binding basis $|\mathbf{r}_\alpha, l\rangle$ that span the

Hilbert-space. Each $|\mathbf{r}_\alpha, l\rangle$ is localized on a site α and carries an internal orbital degree of freedom labeled l . These states are represented as $N_{\text{Sites}} \times N_{\text{Orbs}}$ vectors and satisfy the following relation

$$\langle \mathbf{r}_\alpha, l' | \mathbf{r}_\beta, l \rangle = \delta_{\alpha\beta} \delta_{ll'}. \quad (\text{B2})$$

Using these, we introduce the normalized plane-wave basis set

$$|\mathbf{p}, l\rangle = \frac{1}{\sqrt{N_{\text{sites}}}} \sum_\alpha \exp(i\mathbf{p} \cdot \mathbf{r}_\alpha) |\mathbf{r}_\alpha, l\rangle. \quad (\text{B3})$$

One can now compute the total momentum-resolved spectral function defined as

$$\mathcal{A}(E, \mathbf{p}) = -\frac{1}{\pi} \text{Im} \sum_l \langle \mathbf{p}, l | \mathcal{G}(E) | \mathbf{p}, l \rangle = \sum_l \langle \mathbf{p}, l | \delta(\mathcal{H} - E) | \mathbf{p}, l \rangle. \quad (\text{B4})$$

Appendix C: Quantum geometric tensor in real space

The quantum geometric tensor captures the geometry of quantum states in parameter space. In crystalline systems, Bloch states $|u_n(\mathbf{k})\rangle$ form an eigenbasis of the Hamiltonian due to translational symmetry. However, states within the same band are not orthogonal: $\langle u_n(\mathbf{k}_1) | u_n(\mathbf{k}_2) \rangle \neq \delta(\mathbf{k}_1 - \mathbf{k}_2)$. To quantify how non-orthogonal these states are, Provost and Valle [163] introduced a gauge invariant distance for isolated bands

$$d^{(n)}(\mathbf{k}_1, \mathbf{k}_2) = \sqrt{1 - |\langle u_n(\mathbf{k}_1) | u_n(\mathbf{k}_2) \rangle|^2}. \quad (\text{C1})$$

Considering two states of the same isolated band n distant from $\delta\mathbf{k}$, the infinitesimal interval ds^2 can be written as $ds^2 = G_{\mu\nu}^{(n)}(\mathbf{k}) dk^\mu dk^\nu$, with

$$G_{\mu\nu}^{(n)}(\mathbf{k}) = \langle \partial_\mu u_n(\mathbf{k}) | (1 - |u_n(\mathbf{k})\rangle \langle u_n(\mathbf{k})|) | \partial_\nu u_n(\mathbf{k}) \rangle. \quad (\text{C2})$$

$G_{\mu\nu}(\mathbf{k})$ is the *quantum geometric tensor*, and $\partial_\mu = \partial/\partial k^\mu$ with $\mu, \nu = \{x, y\}$ in two dimensions. Integrating the quantum geometric tensor over the Brillouin zone gives us access to the Hilbert-space volume spanned by the n -th state. The real and imaginary parts of the quantum geometric tensor are called the quantum metric and Berry curvature, respectively [29, 32, 69, 70, 96].

Despite the absence of translational symmetries of aperiodic tilings, it is possible to define a bulk, real-space version of the quantum geometric tensor as [29, 32, 69, 164]

$$G_{\mu\nu} = \frac{2\pi}{\mathcal{A}_b} \sum_{\alpha \in \text{Bulk}} \sum_l \langle \mathbf{r}_\alpha, l | \hat{P} \hat{\mathbf{r}}_\mu \hat{Q} \hat{\mathbf{r}}_\nu \hat{P} | \mathbf{r}_\alpha, l \rangle, \quad (\text{C3})$$

where \mathcal{A}_b is the bulk area, \hat{P} is the projector over occupied states, $\hat{Q} = 1 - \hat{P}$ is the projector onto unoccupied states and $\hat{\mathbf{r}}_\mu$ is defined as

$$\hat{\mathbf{r}}_\mu = \begin{cases} \hat{X} & \text{if } \mu = x, \\ \hat{Y} & \text{if } \mu = y. \end{cases} \quad (\text{C4})$$

To discuss the trace inequality [111–116], as we do in the main text, it is important to normalize $G_{\mu\nu}$ consistently for all ℓ . We achieve this by normalizing bulk-averaged quantities over a Voronoi tessellation [165, 166] of the system at each ℓ , see Fig. S2. Here, the bulk region is defined via Voronoi cells centered on lattice sites within a finite window, and the bulk area \mathcal{A}_b is the sum of their individual areas. By using the Voronoi tessellation we can conveniently account for each of the atomic site's area that contributes to \mathcal{A}_b .

The quantum metric computed in the main text is then defined as the sum of the diagonal components of the quantum geometric tensor

$$G = \text{Re}[G_{xx} + G_{yy}]. \quad (\text{C5})$$

From Eq. (C3) one can define a local quantum metric as:

$$g_{\mathbf{r}_\alpha} = 2\pi \text{Re} \sum_l \langle \mathbf{r}_\alpha, l | \hat{P} \hat{X} \hat{Q} \hat{X} \hat{P} + \hat{P} \hat{Y} \hat{Q} \hat{Y} \hat{P} | \mathbf{r}_\alpha, l \rangle. \quad (\text{C6})$$

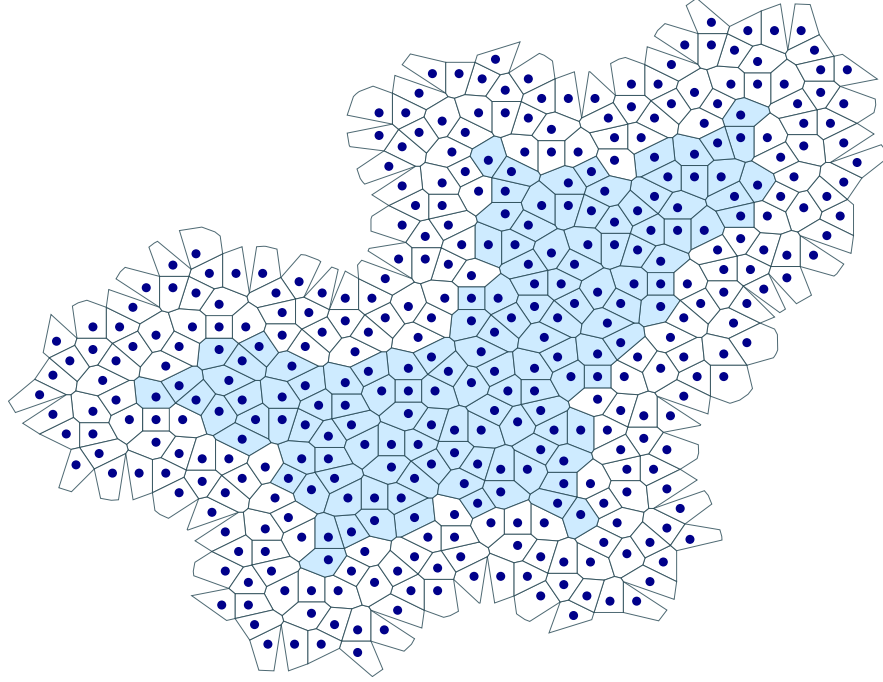


Figure S2. Voronoi tessellation of the lattice obtained for $\ell = 0.5$. The Voronoi cells corresponding to bulk sites are highlighted in light blue. The bulk area \mathcal{A}_b corresponds to the sum of all the areas corresponding to individual blue cells.

The quantum metric is then defined as the normalized sum over the bulk of the local quantum metric Eq. (C6)

$$G = \frac{1}{\mathcal{A}_b} \sum_{\alpha \in \text{Bulk}} g_{\mathbf{r}_\alpha}. \quad (\text{C7})$$

The quantum geometric tensor encodes important geometric and topological properties of the electronic structure: The quantum metric quantifies the spatial spread of the occupied states: $G \sim \langle \mathbf{r}^2 \rangle - \langle \mathbf{r} \rangle^2$ and is related to the localization properties of Wannier functions [71, 72].

Analogously, the much more commonly studied local Chern marker is defined by the antisymmetric, imaginary part of the quantum geometric tensor [70, 96]. Its bulk average, as defined in the main text below Eq. (2), converges to the Chern number of filled states, even in systems lacking translational symmetry.

Appendix D: Spectral localizer gap and choice of κ

In this section, we justify the choice of the parameter κ used to generate Fig. 3 via the spectral localizer [103–106], whose definition we repeat here for convenience

$$\mathcal{L} = (\hat{\mathcal{H}} - E_0 \mathbb{1}) \sigma_z + \kappa \left[(\hat{X} - x_0 \mathbb{1}) \sigma_x + (\hat{Y} - y_0 \mathbb{1}) \sigma_y \right]. \quad (\text{D1})$$

The parameter κ balances the typical energy scales of the Hamiltonian \mathcal{H} compared to those of the position operators \hat{X} and \hat{Y} . If κ is chosen too small, the localizer \mathcal{L} becomes approximately $(\hat{\mathcal{H}} - E_0 \mathbb{1}) \sigma_z$, whose spectrum is symmetric around zero. Because of this symmetry the signature vanishes, yielding a trivial topological invariant. Conversely, if κ is chosen too large, the localizer is dominated by the position operators and effectively decouples from the Hamiltonian, again resulting in a trivial invariant. Therefore, κ must be chosen so that the Hamiltonian and the position operators contribute comparably to the localizer, ensuring the computation captures the correct topological features.

To find a suitable value of κ , it is convenient to compute the localizer gap at different energies for different values of κ [106]. The localizer gap is defined as the magnitude of the smallest eigenvalue in absolute value, $\min(|\lambda|)$ where $\lambda \in \text{Sp}(\mathcal{L})$. For a given matrix A , $\text{Sp}(A)$ denotes the set of all the eigenvalues of A or spectrum of A . Because the

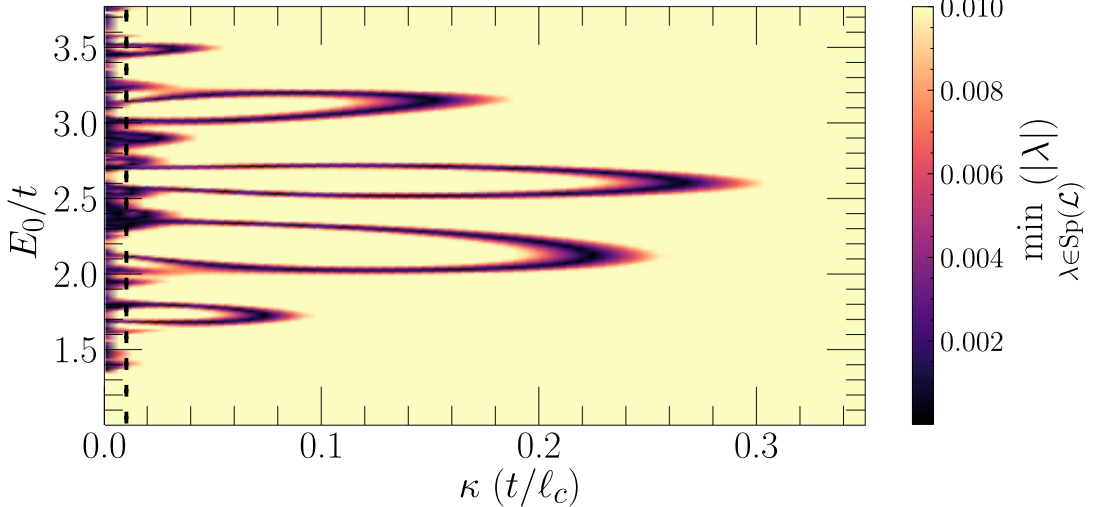


Figure S3. Localizer gap of the spectral localizer Eq. (D1) as a function of the reference energy E_0/t and the parameter κ , measured in units of t/ℓ_c . Here $\ell_c = 1$ is the side of the *Comet* tile, see Fig. 1a, and sets our unit length. We compute in the bulk of the system, at a position x_0, y_0 chosen by computing the geometric mean of the site's coordinates, for $\ell = 0.5$ and $M/t = 0.5$. The vertical dashed black line corresponds to the value of κ used in the main text. For $E_0/t = 2.65$, the energy set by E_F at this ℓ in Fig. 3, we are within a bubble with a large localizer gap that is well defined for several orders of magnitude in κ .

invariant can only change when the localizer gap closes, the magnitude of the localizer gap attests to the robustness of a given phase computed for a given choice of parameters (κ, x_0, y_0, E_0) . A large gap, extended in parameter space, signifies a stable phase [105, 106, 167, 168]. In this sense the localizer gap acts analogously to the band-gap of crystalline systems. In practice, for a given system size there is not a single value of κ but rather a window of values of κ that capture well the topologically robust properties of the system [106].

In Fig. S3 we plot the localizer gap as a function of both κ and E_0/t for x_0 and y_0 chosen in the bulk of the system, by computing the geometric mean of the site's coordinates. We observe the emergence of distinct bubbles where the localizer gap is large, similar to other localizer studies [105, 106, 167–169]. These bubbles correspond to the regions in parameter space where both the Hamiltonian and the position operators enter meaningfully the calculation of the spectral localizer. We have checked that, by selecting a value of κ such that the energy of interest lies within one of these bubbles, we ensure that the invariant computed via the spectral localiser at a given energy approximately coincides with the bulk average of the local Chern marker at the same energy. Furthermore, we observe that the bubble at $E_0/t = 2.65$, the energy set by E_F at this ℓ in Fig. 3, is particularly extended, which ensures the robustness of the calculation with respect to different choices of the parameter κ .